ASME Journal of Mechanisms and Robotics
Online journal at:
https://asmedigitalcollection.asme.org/mechanismsrobotics

Magnetically-Actuated Endoluminal Soft Robot With Electroactive Polymer Actuation for Enhanced Gait Performance

Jake A. Steiner
Dynamic Autonomous Robotics Lab,
Department of Mechanical Engineering,
University of Utah,
Salt Lake City, UT 84112

William S. Nagel
Department of Robotics Engineering,
Widener University,
Chester, PA 19013

Kam K. Leang[1]
Fellow ASME
Dynamic Autonomous Robotics Lab,
Department of Mechanical Engineering,
University of Utah,
Salt Lake City, UT 84112
e-mail: kam.k.leang@utah.edu

Endoluminal devices are indispensable in medical procedures in the natural lumina of the body, such as the circulatory system and gastrointestinal tract. In current clinical practice, there is a need for increased control and capabilities of endoluminal devices with less discomfort and risk to the patient. This paper describes the detailed modeling and experimental validation of a magneto-electroactive endoluminal soft (MEESo) robot concept that combines magnetic and electroactive polymer (EAP) actuation to improve the utility of the device. The proposed capsule-like device comprises two permanent magnets with alternating polarity connected by a soft, low-power ionic polymer-metal composite (IPMC) EAP body. A detailed model of the MEESo robot is developed to explore quantitatively the effects of dual magneto-electroactive actuation on the robot's performance. It is shown that the robot's gait is enhanced, during the magnetically-driven gait cycle, with IPMC body deformation. The concept is further validated by creating a physical prototype MEESo robot. Experimental results show that the robot's performance increases up to 68% compared to no IPMC body actuation. These results strongly suggest that integrating EAP into the magnetically-driven system extends the efficacy for traversing tract environments.

[DOI: 10.1115/1.4066130]

Keywords: *compliant mechanisms and robots, soft robots*

1 Introduction

New endoluminal robotic systems aim to empower clinicians to reach deeper into the human body and minimize patient discomfort or risk of damage during therapeutic and diagnostic procedures. Considering the gastrointestinal (GI) tract, enteroscopy and colonoscopy exams are essential in screening procedures to catch problems early, thereby leading to better outcomes [1,2]. However, there are challenges in the procedures due to discomfort and invasiveness [3,4]. Further, the small intestine is largely unreachable with push-based methods without significantly increasing the risk to the patient, where approaches mainly rely on uncontrolled pill-shaped capsules [5]. Thus, controlled access through the use of capsule-like methods [6] is highly desirable. This is the same for the circulatory system where push-based procedures are common, involve pushing a catheter from the proximal end into the body's vasculature [7,8]. To reach the desired site, multiple catheters need to be inserted and navigation is a challenge. There is a risk of damage, such as perforation, to the vessel from unavoidable pressure on the lumen surfaces [9]. Thus, additional control is desired for these procedures to, for example, assist in insertion, reduce forces on lumen walls, or enhance the traversal speed of the capsule.

This paper presents the detailed modeling and experimental validation of novel magneto-electroactive endoluminal soft (MEESo) robot that has the potential to improve the utility (such as locomotion ability) of endoluminal robotic devices. The MEESo robot, illustrated in Fig. 1, utilizes a combination of magnetic and electroactive polymer (EAP) actuation to affect its inchworm-like gait. This concept was first introduced by our group in preliminary work through very basic modeling [10]. Specifically, the robot comprises two permanent magnets affixed coaxially with alternating polarity to an EAP body, in this case, made from an ionic polymer-metal composite (IPMC). The primary driving force of the robot is from magnetic actuation induced by a rotating actuation magnet located outside the patient [11]. The robot's electroactive polymer body influences the robot's deformation while traversing a lumen environment, resulting in greater gait control. The MEESo robot actuation methods are simple in terms of design and fabrication, lending to the possibility of incorporating the concept into capsule-like devices for use in the GI tract or integrated into catheter devices for use in the circulatory system.

Prior endoluminal robot designs have utilized a variety of actuation mechanisms. Many methods are mechanically complex; thus scaling them to work across various lumen sizes of the natural lumina is nontrivial. These devices include robots that use motors to drive the locomotion, such as the legged robots proposed in Refs. [12,13] or the vibration-based robot in Ref. [14]. On the other hand, endoluminal robots utilizing external actuation and artificial muscle materials often benefit from simpler design and straightforward scaling.

External actuation via inter-magnetic forces and torques has been applied across a large scale of robots for use in the GI tract down to the circulatory system. In the circulatory system, magnetic actuation has primarily been used to help steer catheters deeper into the body [15–18]. For the GI tract, magnetically-actuated capsule-like robots have been proposed to traverse through the intestines using a periodic gait. These methods often rely on magnetic torque from an actuation field to produce the gait cycle. Magnetic torque scales better with distance from the magnetic field source than force. Jung et al. [19] have produced a magnetic worm-like endoluminal robot; it may not be trivial to reduce in size to work in the

---

[1] Corresponding author.

Contributed by Mechanisms and Robotics Committee of ASME for publication in the Journal of Mechanisms and Robotics. Manuscript received January 23, 2024; final manuscript received July 22, 2024; published online September 2, 2024. Assoc. Editor: Chin-Hsing Kuo.

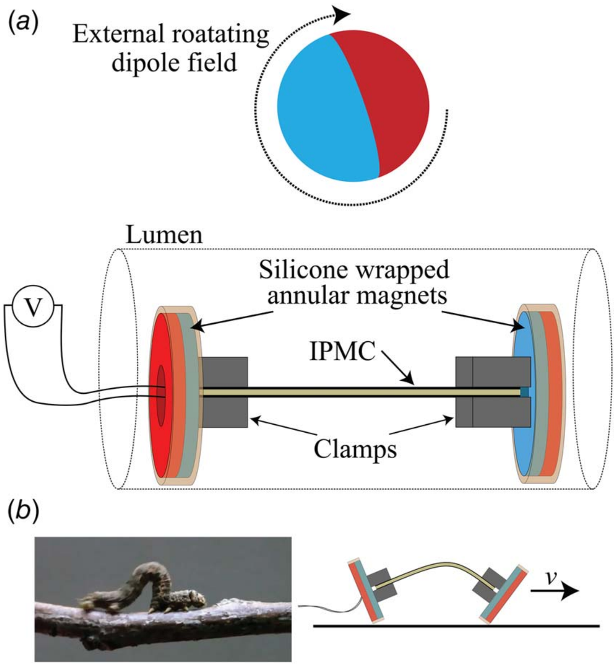

Fig. 1 The MEESo robot concept: (*a*) robot locomotion is achieved with magnetic and electroactive actuation via a rotating dipole actuation field and an ionic polymer-metal composite actuator (IPMC), and (*b*) the robot's gait is biomimetic, resembling that of an inchworm caterpillar. The IPMC actuator enables increased control of the body deformation, which creates the contraction and expansion phases of the gait cycle.

vasculature due to the complexity of the fabrication. Spiral-based capsule methods such as Ref. [20] can be scaled down to the size of the vasculature, but their use on the distal end of a catheter or flexible shaft endoscope may not be feasible due to the constant rotation. The MEESo robot proposed in this work uses an inchworm magnetically driven gait to create mechanically simple locomotion and requires no rotating joints. It is also well suited to scale to various lumen sizes [21]. The MEESo robot behavior is enhanced with a second form of actuation from an electroactive polymer via an ionic polymer-metal composite actuator.

Ionic polymer-metal composites are a particular variant of electroactive polymers that exhibit large strain when an electric potential is applied or produce an electrical signal when mechanically deformed [22]. Compared to other electroactive polymers, such as dielectric elastomers actuators [23,24] or hydraulically amplified self-healing electrostatic actuators [25,26], IPMCs require lower voltages for actuation to achieve relatively fast and large deformations. The input voltage for IPMCs is typically less than 3 V to avoid degradation through electrolysis [27,28]. IPMCs have been deployed in a wide variety of soft robotic and biomimetic devices [29–32]. Furthermore, IPMCs can be integrated into soft devices to serve as low-power, highly deformable sensors [33–35]. In the current research toward medical applications, IPMC actuation has been used in catheters, where the composite is often affixed to the distal end of the instrument and used to assist in navigating the device through endoluminal channels [36–40]. However, to the best of the authors' knowledge, IPMCs and similar electroactive polymer actuators have not been used in conjunction with external magnetic actuation for improved robot performance through actively enhanced body deformations during the gait cycle.

This paper presents a novel MEESo robot concept that combines an endoluminal magnetic actuation method with an actively deformable IPMC body, which was originally presented in Ref. [10]. It is believed that the dual actuation of the MEESo robot will lead to a device that can outperform devices using a singular actuation method (i.e., through magnetic actuation alone). The fabrication and the first experimental demonstration of the robot concept are presented. The MEESo robot is intended to have applications in tethered controllable capsule-like robots for the GI tract or integrated into a catheter-like device to aid in the insertion from the distal end in the circulatory system.

The main contributions of the work are, first, a significantly improved model from preliminary work shown in Ref. [10]; this work presents a 3D model of the MEESo robot and environment, and considers the dynamics of the robot's gait in determining the traversal behavior of the device. Second, the first functioning MEESo robot prototype is fabricated and tested to validate the benefits of magneto-electroactive actuation concept. The purpose of these experiments is to demonstrate the overall feasibility of the EAP-enhanced magnetic robotic concept, where a few basic IPMC body actuation methodologies (i.e., constant and gait-dependent driving voltages) are considered.

The remainder of the paper is organized as follows. First, the physics governing the MEESo robot's motion is presented in Sec. 2. Second, in Sec. 3, a 3D model is created and the beneficial effects of electroactive actuation are demonstrated in simulation. Then in Sec. 4, a MEESo robot is fabricated and tested, where simulation and physical experimental results are presented. Results are discussed in Sec. 5, followed by concluding remarks in Sec. 6.

2 MEESo Actuation Physics

The MEESo robot leverages two actuation methods: (1) magnetic actuation that induces an inchworm-like gait and (2) electroactive polymer actuation that further deforms the robot's body for enhancing locomotion. A rotating magnetic field is generated externally from the lumen and interacts with permanent magnets embedded in the robot's feet. The robot's feet alternate between sticking and slipping as the body contracts and expands through deformation from the imposed torques of the nonuniform rotating magnetic field, which results in net forward motion of the robot through a lumen environment. Thus, it is the contortion of the robot's body, traditionally imposed solely by this external magnet, which results in the mobility of the robot. The new concept of the MEESo robot is the addition of an electroactive polymer in (or consisting entirely of) the robot's body, enabling increased control over the body deformation and thus the traversal speed of the robot. The physics that govern the magnetic and electroactive material actuation modalities are described in the following.

2.1 Magnetic Actuation Model.

Magnetically-actuated devices, such as the robot configuration shown in Fig. 1(*a*), rely on the inter-magnetic forces and torques on a magnet in an actuation magnetic field. The actuation field $\mathbf{B}$ due to a dipole source $\mathbf{M}$ at position $\mathbf{R}$ is defined as

$$\mathbf{B} = \frac{\mu_0}{4\pi}\frac{3(\mathbf{M}\cdot\hat{\mathbf{R}}) - \mathbf{M}}{\|\mathbf{R}\|^3} \tag{1}$$

where $\mu_0 = 4\pi \times 10^{-7}\ \mathrm{T}\cdot\mathrm{m/A}$ is the magnetic permeability of free space and $\hat{\mathbf{R}}$ is a unit vector in the direction of position $\mathbf{R}$ [41]. Approximating a magnetic source as an ideal dipole source is perfectly accurate for spherical magnets and a good approximation of other shapes at distances sufficiently far from the source [42]. Furthermore, magnetic shapes that are not well approximated by the dipole model can be divided into regions that are and their effects summed. The forces and torques on a dipole $\mathbf{M}$ in an actuation field $\mathbf{B}$ are defined as

$$\mathbf{F} = (\mathbf{M}\cdot\nabla)\mathbf{B} \tag{2}$$

and

$$\boldsymbol{T} = \mathbf{M}\times\mathbf{B} \tag{3}$$

The MEESo robot relies on the nonuniform field of a dipole actuation magnet to locomote. From prior work, it is known that intermagnetic torques primarily drive the robot. The dipole field of the actuation magnet imposes nonsymmetric torques on the two opposing polarity magnets in the feet of the robot. As the actuation magnet rotates, the torques on the embedded magnets in the robot cause the body to contract and expand throughout the gait cycle due to the deformation of the body segment. Because the torques are nonsymmetric, the feet of the robot alternate sticking and slipping actions while the body deforms, leading to an inchworm-like gait. Interested readers can find a more detailed description of the robot's gait in Refs. [11] and [21].

2.2 Electroactive Polymer Model. An IPMC comprises an ionic polymer, for instance, Nafion, sandwiched between two noble metal electrodes, such as gold or platinum [43]. When an electric potential is applied to the electrodes, ion migration and redistribution cause a bending deformation to occur in the material. Specifically, IPMC actuation can be thought of as a "swelling" in the polymer resulting from a hydraulic effect where hydrated ions migrate due to electrophoresis. Particles accumulate at the cathode side of the IPMC, resulting in a bending deformation as depicted in Fig. 2.

For an IPMC, the total stress experienced by the polymer ($\boldsymbol{\sigma}_{\text{IPMC}}$) can be approximated by the sum of the external stress on the polymer backbone from external loading ($\boldsymbol{\sigma}_{\text{L}}$), the osmotic stress caused by the redistribution of water molecules in the polymer ($\boldsymbol{\sigma}_{\text{O}}$), and the electrostatic stress resulting from an imbalanced charge density ($\boldsymbol{\sigma}_{\text{V}}$) [44], i.e.,

$$\boldsymbol{\sigma}_{\text{IPMC}} = \boldsymbol{\sigma}_L + \boldsymbol{\sigma}_O + \boldsymbol{\sigma}_V \tag{4}$$

The osmotic stress is expected to be small relative to the other stresses, so they are considered negligible here ($\boldsymbol{\sigma}_{\text{O}} \approx 0$). Furthermore, the external stress on the IPMC is captured by the mechanical deformation of the MEESo robot (gait approximation), thus the electrostatic stress needs to be determined to account for the IPMCs effects on the total MEESo robot locomotion.

The charge imbalance of the IPMC, $\boldsymbol{\rho}$, is given as the divergence of the electric field, $\mathbf{E}$, in the IPMC, which is defined to be the negative gradient of the electric potential, $\boldsymbol{\phi}$, hence

$$\boldsymbol{\rho} = \nabla \cdot c_e \mathbf{E} \tag{5}$$

$$\mathbf{E} = -\nabla \boldsymbol{\phi} \tag{6}$$

where c_e is the effective dielectric constant of the polymer. Assuming that this dielectric constant is uniform throughout the material, the electrostatic stress of the IPMC can be expressed as

$$\boldsymbol{\sigma}_V = c \nabla^2 \boldsymbol{\phi} \mathbf{I} \tag{7}$$

Here $\mathbf{I}$ is the identity tensor since the Laplacian of the electric potential is a scalar value. Variable c represents a constant combining the dielectric constant and a scaling factor relating the electrostatic stress and charge density.

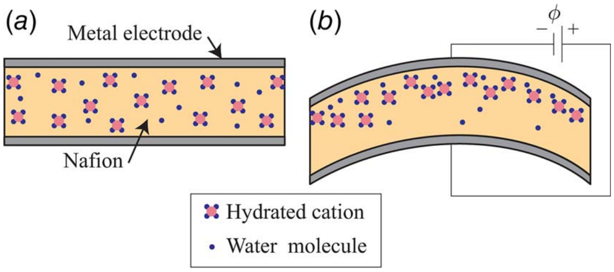

Fig. 2 Illustration of IPMC actuation: (*a*) unactuated IPMC, consisting of a Nafion membrane with noble metal electrodes and (*b*) when an electric potential, ϕ, is applied to the electrodes, hydrated cations in the polymer are attracted to the cathode. This effect cause the IPMC to bend toward the anode.

If an electric potential of magnitude V is applied, and assumed constant throughout each electrode, the moment applied to the IPMC due to the electrostatic stress, τ_V, is found by integrating about the cross-sectional area A of the material with thickness x, hence

$$\tau_V = \int_A x \boldsymbol{\sigma}_V dA = m_0 V \tag{8}$$

Thus, a constant moment is experienced in the material with a magnitude proportional (value m_0) to the applied potential V. This proportionality can be determined through the physical parameters of the IPMC [44]; however, this work experimentally determines the value of m_0 through measured tip displacement of the IPMC strip used to construct the MEESo robot.

Previous work has analyzed the locomotion of a passive soft robot, showing that the contortion of the soft body directly contributes to the step size of the robot, and consequentially the inherent velocity of the device [11,21]. Therefore, by incorporating EAP actuation into the soft body of the device and directly influencing the shape of the robot during operation, the traversal speed can be improved throughout the gait by synchronizing the IPMC actuation voltage (and consequently the applied moment τ_V according to Eq. (8) above) with the external magnet's orientation. It is hypothesized that introducing this distributed moment through the robot body increases the body deformation through the anchor-pull and push phases of the gait, allowing for more displacement to occur in the step. This expected behavior will be verified through simulations in Sec. 3, as well as physical experiments on example prototype device in Sec. 4.

3 Simulation and Experimental Results

The MEESo robot is first modeled in a 3D simulation environment to determine the appropriate actuation methods to experiment on a physical robot.

3.1 Methods. The 3D rigid-body model of the soft robot is shown in Fig. 3(*a*). The model is created using WEBOTS, an open-source mobile robot simulation software package [45]. The robot has cylindrical feet that represent the embedded magnets. Rectangular prism clamps that are rigidly attached to the feet hold the thin IPMC body.

The flexible IPMC body is modeled by N discretized rigid elements connected by $n = N - 1$ torsional springs. This model approximates the continuum mechanics of the body. The spring constant of each torsional spring is given by

$$k = \frac{nEI}{L} \tag{9}$$

where L is the length of the beam, E is the Young's modulus, and I is the second moment of area of the beam in bending.

From the IPMC model described in the previous section, the stress generated in the composite material with an applied electric potential can be described by a constant moment along the body. This moment can be determined based on geometric properties of the IPMC actuator or experimentally found based on its displacement when voltage is applied. For simplicity, nonlinear effects present in the material (e.g., back relaxation) are ignored, and it is assumed that the moment generated by the IPMC is linear with applied voltage (constrained between ±3 V). The bending moment for the IPMC body is experimentally determined to be $m_0 = 0.0193\,\text{nNm/V}$ based on Eq. (8), where the numerical curvature of an IPMC is tuned through the value of m_0 such that it matches the experimentally measured curvature of the material. The constant bending moment of the IPMC, τ_v, is represented as

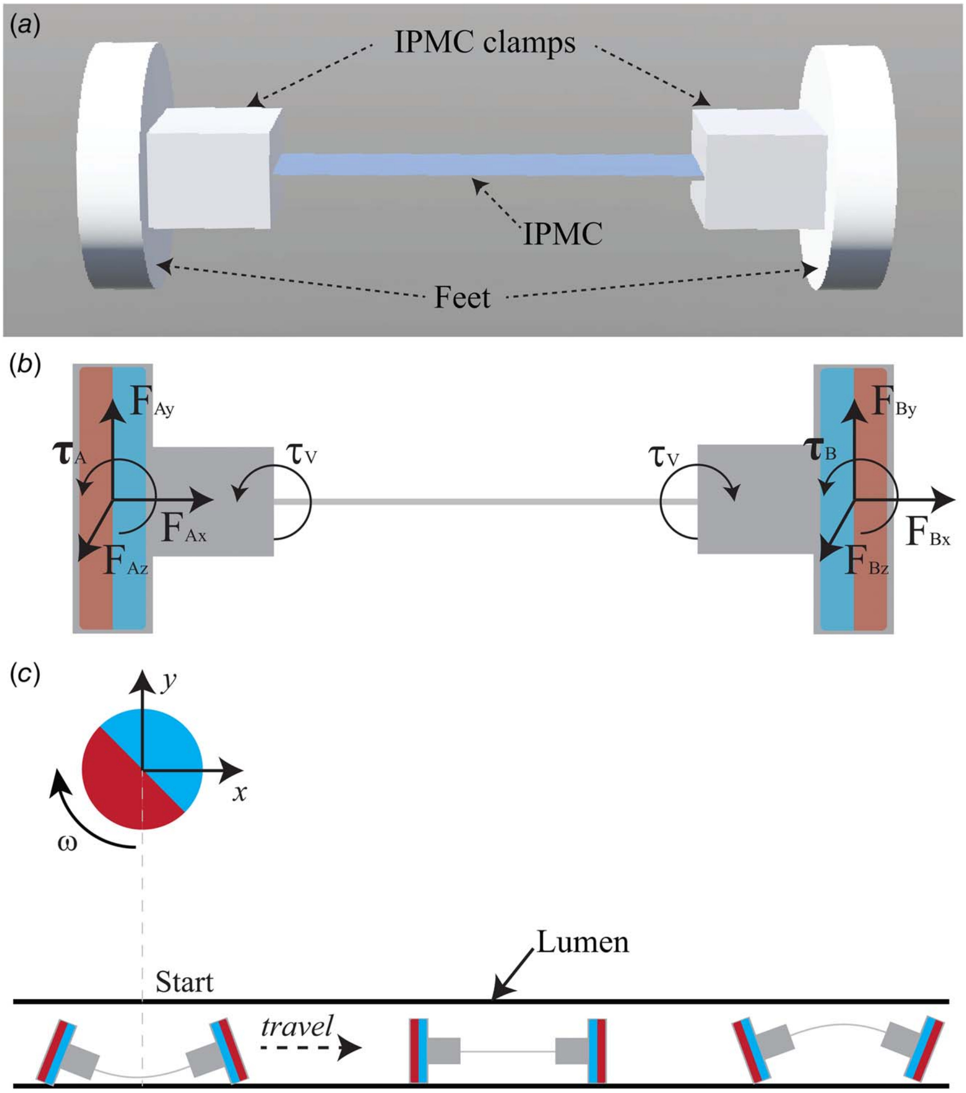

Fig. 3 MEESo robot model and simulation setup: (*a*) a screenshot of the modeled robot in the WEBOTS mobile robot simulator, (*b*) an illustration of the MEESo robot with imposed inter-magnet forces and torques and electroactive torques from the polymer body, and (*c*) simulation setup: the robot starts directly underneath the actuation magnet that rotates clockwise, driving the robot to the right (+x)

equal and opposite torques applied at both ends of the body section, which can be seen in Fig. 3(*b*).

The inter-magnetic forces and torques between the three magnets in the model are calculated by Eqs. (2) and (3). At each time-step of the simulation, the forces and torques on the robot from both actuation methods are applied, again illustrated in Fig. 3(*b*).

The experimental setup of the simulation is depicted in Fig. 3(*c*). The actuation magnet rotates at 1 Hz about the $-z$-axis in a fixed location. The dipole of the actuation magnet starts at 0 deg aligned with the x-axis. The robot starts in the $-x$ region and travels in the $+x$-direction. The robot's position is recorded from $x = 0$ mm to $x = 60$ mm. With this actuation configuration, the robot's inchworm gait leads to travel in the positive x-direction. For such an experimental setup, the robot is expected to exhibit the fastest traversal speed when directly underneath the external rotating magnet, as the inter-magnetic torques will result in the largest body deformations based on the nonuniform magnetic field [21]. As the robot moves further away from the rotating-actuating magnet, traversal speed decreases.

In addition to the magnetic actuation, the IPMC is also given an actuation voltage V_{act} to enhance the robot's locomotion. As the optimal IPMC signal for the best performance increase is currently unknown, constant and alternating voltages are investigated here. To add variability to the simulation, the robot's initial position for each trial is varied along the lumen. Also, Gaussian noise with a standard deviation of 2 mm and 2 deg is added to the actuation magnet's position and angle, respectively, during the trials. Each actuation scenario is simulated for 30 trials to determine the average behavior. It is noted that the scenario of IPMC-only actuation (i.e., there is no external rotating magnetic field) is not explored, as these devices are not realistically capable of producing forces large enough to traverse a lumen environment. Instead, the purpose of incorporating IPMC body deformation is to enhance the gait of the traditional magnetically-actuated inchworm-like robot device.

It is worth noting, also, that alternative smart materials can be integrated into the simulation. The appropriate actuation model must be considered, similar to the process described above.

3.2 Results. First, actuating the IPMC with a constant voltage is examined. The simulation considers a segmented robot body of

$N = 15$ with actuation voltages in the range of ± 3 V with 1 V increments, where $V_{act} = 0$ V is the IPMC is left inactive. Results of the simulation are shown in Fig. 4(*a*), where the robot's traversal speed is plotted against the distance traveled by the robot. Based on these simulations, the robot tends to travel faster when the body is biased concave with respect to the ground (i.e., $V_{act} > 0$), while the opposite bias tends to slow the robot. The effects of these trends increase as the bias voltage magnitude increases. The robot speed directly under the actuation magnet can be increased or decreased by approximately 32% and 57% on average, respectively.

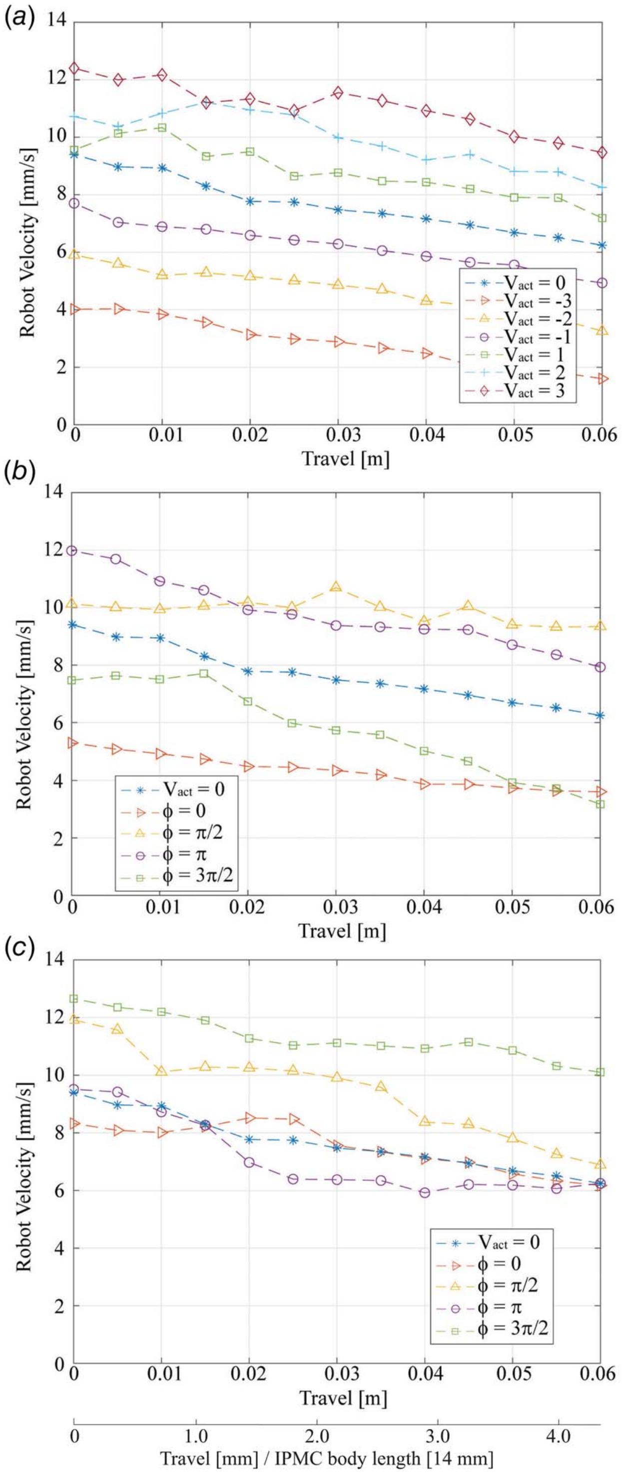

Fig. 4 Results for the dual-actuated magneto-electroactive robot, where magnetic actuation is operated at 1 Hz: (*a*) constant-voltage electroactive actuation (V_{act}), (*b*) sinusoidal-wave electroactive actuation $V_{act} = 3\sin(2\pi f t + \varphi)$, where the phase shift φ is adjusted in $\pi/2$ rad increments. $V_{act} = 0$ shown for reference, and (c) square-wave electroactive actuation $V_{act} = 3/2(\text{sign}(\sin(2\pi f t + \varphi)) + 1)$. $V_{act} = 0$ shown for reference.

Next, the effects of synchronizing the IPMC actuation signal with the magnet's rotation are investigated. Because the IPMC effectively provides an additional torque that allows for more or less contortion in the MEESo robot's body throughout the gait cycle, it is reasonable to expect a periodic signal to coordinate these torques with the actuation magnet's orientation. The actuation voltage is defined as

$$V_{act} = 3\sin(2\pi f t + \varphi) \tag{10}$$

where $f = 1$ Hz is the frequency of the actuation magnet, t is the time elapsed since the start of the trial, and φ is the phase shift of the IPMC sinusoidal-wave actuation. (Note: because the magnet starts at a specific orientation, this is equivalent to synchronizing the IPMC actuation signal with the magnet's orientation.) Four evenly spaced phase shifts are examined: $\varphi \in \{0, \pi/2, \pi, 3\pi/2\}$ rad. The results compared to no actuation ($V_{act} = 0$) are presented in Fig. 4(*b*). Similar to the constant V_{act} results, the MEESo robot's lumen traversal speed can be increased and decreased using this actuation method, indicating that synchronizing the electroactive modality with the actuation magnet's rotation is necessary for periodic electroactive actuation signals. In particular, for the actuation methods that improve the robot's speed, $\varphi = \pi$ and $\pi/2$ rad, the IPMC actuation compliments the magnetic actuation, helping the robot contract greater per gait cycle. The robot's speed is improved as much as 28% at $x = 0$. Conversely, $\varphi = 0$ and $3\pi/2$ rad, decrease the robot's velocity due to a mismatch between the effects of IPMC actuation and the magnet-induced gait.

Since the concerned in this work is primarily with benefiting the gait, it can be seen that the best sinusoidal-wave actuation method did not improve the performance as much as DC voltage actuation ($V_{act} = 3$ V). This shows that the negative cycle of the sinusoidal signal does not benefit the magnetic gait. The robot is only benefited by IPMC actuation assisting in the contracting phase, bringing the feet closer together. The last signal type tested aims to maximize IPMC actuation during the beneficial contracting portion of the gait and leave it dormant during the expanding phase.

The effects of electroactive actuation from a square-wave signal between $V_{act} = 3$ V and $V_{act} = 0$ V is simulated. Specifically, the signal is given as

$$V_{act} = 3/2(\text{sign}(\sin(2\pi f t + \varphi)) + 1) \tag{11}$$

where the signum function, $\text{sign}(\cdot)$, is defined as

$$\text{sign}(x) = \begin{cases} 1 & \text{if} x \geq 0 \\ -1 & \text{if} x < 0 \end{cases} \tag{12}$$

The four phase shifts used in the sinusoidal-wave simulations are investigated. The results are shown in Fig. 4(*c*). What is seen from these results is positive IPMC voltage, or an upward bend, can not do much to slow the magnetically-actuated robot down, but it can be beneficial to increase the robot's speed. The phase shift of $\varphi = 3\pi/2$ rad shows increases in traversal velocity similar to the DC voltage actuation case, with velocity increasing about 35% at $x = 0$. This actuation only requires half the active time of the IPMC but produces similar performance to the best DC voltage actuation and better performance than all sinusoidal-wave signals tested.

4 Physical Experiments and Results

A physical MEESo robot was fabricated for testing. Based on the simulation results, two magneto-electroactive actuation schemes are chosen to compare to purely magnetic actuation: a constant (DC) bias signal and a synchronized periodic signal. The two actuation methods tested are a constant voltage of +3 V and a square-wave actuation signal with $\varphi = 3\pi/2$ rad.

4.1 Methods.

The physical experimental setup is shown in Fig. 5(*a*). The setup matches the configuration in the simulation environment. The lumen environment is a half-cylindrical trough with a diameter of 14 mm, shown in Fig. 5(*b*). The half-cylinder is selected to represent a lumen environment because the gait of the MEESo robot does not require a ceiling for propulsion [21].

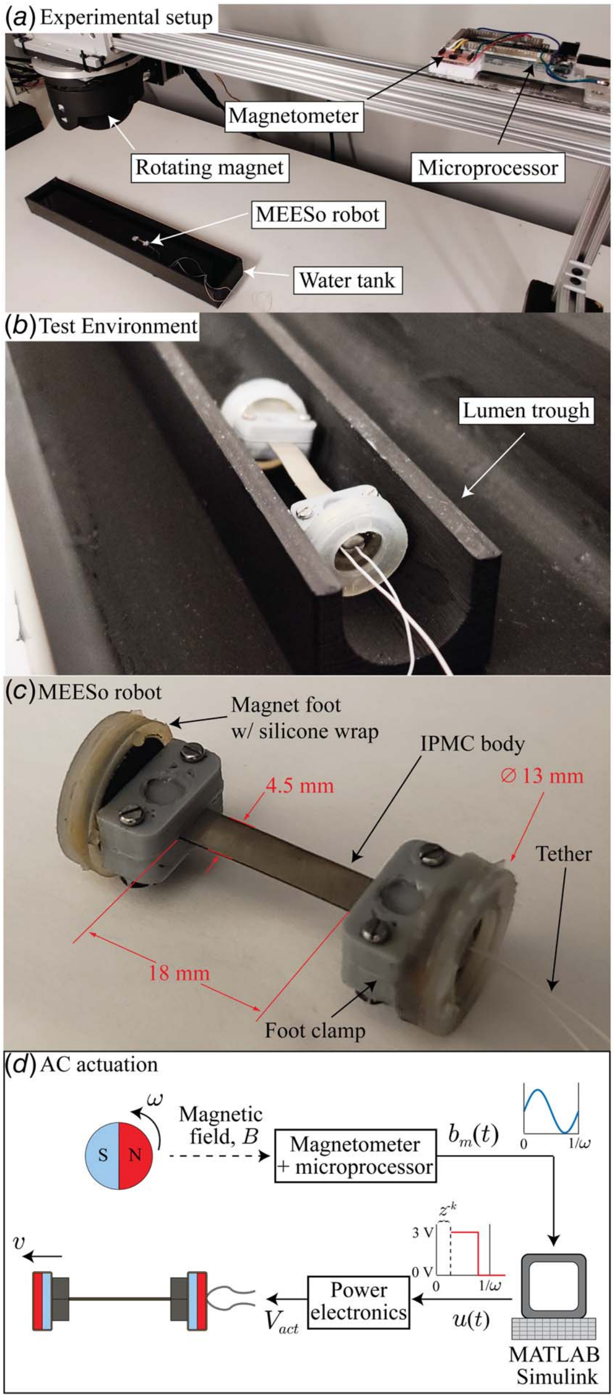

Fig. 5 (*a*) **Experimental setup for MEESo robot validation, (*b*) the MEESo robot in the environment, (*c*) MEESo robot consists of magnetic feet and an IPMC body, and (*d*) signal flow diagram for applying an AC actuation signal to the IPMC body synchronized with the rotating magnet orientation**

Also, the configuration allows for motion capture cameras to easily record the movement of the robot during experiments for performance quantification. The environment and MEESo robot are submerged in water. The fabricated MEESo robot is shown in detail in Fig. 5(*c*). The robot has annular permanent magnets (K&J Magnetics R842-N52) wrapped in silicone for the feet. The silicon is used here to extend the life of the experimental robot as it interacts with the hard plastic trough, and can be accounted for by adjusting the coefficient of friction between the two surfaces in simulation. The IPMC body is held in place by plastic clamps affixed to the feet. The wire tether for electroactive actuation is passed through the center of the annular magnet.

To synchronize the MEESo IPMC body actuation signal with the actuation magnet's rotation, a magnetometer (Melexis MLX90393) is used to sense the actuator magnet's orientation during operation. This sensor is arranged such that the detected field induces a sinusoidal response in the sensor, detected by a microcontroller (Arduino Due). The signal is sent directly to a data acquisition system (National Instruments PCI-6221) with a sampling frequency of 1 kHz (sample period $T_s = 0.001$ s). MATLAB SIMULINK real-time is used to take this sinusoidal response from the magnetometer, $b_m(t)$, with voltages within the range of 0.55–2.75 V, and produce a square-wave signal $u(t)$ with voltages of either 0 V or 3 V. Because the actuation magnet is operated at a constant rotational velocity, this signal is also delayed by $k = 250$ time-steps (0.25 s) such that the resulting square wave's high-low pattern matches that of the best-performing scenario observed in simulation $\varphi = 3\pi/2$ rad. Thus, the operation to convert the sinusoidal magnetometer reading to an offset square wave becomes

$$u(t) = 1.5\left[\mathrm{sign}\left(b_m(t - kT_s) + \frac{3.3}{2}\right) + 1\right] \tag{13}$$

Lastly, this low-power signal is conditioned using an LM675 power op-amp to obtain V_{act} that can produce the current necessary to produce deformation in the electroactive polymer. These steps are depicted in Fig. 5(*d*).

4.2 Results.

The physical experimental results are presented in Table 1. The two IPMC actuation methods are experimentally implemented: (1) constant-voltage (DC) actuation denoted by "DC Act." and (2) square-wave actuation denoted by "SQW Act." The baseline no IPMC actuation case is denoted by "No Act." For each configuration, five trials are conducted to observe average performance trends. Each method is tested in order (No Act., DC Act., and SQW. Act), and this is repeated five times. Results show the time (with 95% confidence) for the MEESo robot to reach three distances in the lumen: 20 mm, 40 mm, and 60 mm. A time-lapse view of a MEESo robot being experimentally driven solely by the external magnet is compared to a constant 3 V potential (DC Act.) on the IPMC body during magnetic actuation in Fig. 6.

5 Discussion

Dual actuation on the MEESo robot is first tested in simulation. From the simulation results (Sec. 3.2), two electroactive methods were selected to validate the improvements observed on a physical robot. In physical experiments, it was shown that activating the

Table 1 Experimental data results: average time to distance with 95% confidence interval

	No Act.	DC Act.	SQW Act.
Time to 20 mm (s)	9.4 ± 2.6	3.0 ± 1.1	4.7 ± 3.1
Time to 40 mm (s)	15.8 ± 3.6	7.9 ± 2.1	10.0 ± 4.1
Time to 60 mm (s)	21.1 ± 5.6	15.1 ± 5.6	16.1 ± 6.7

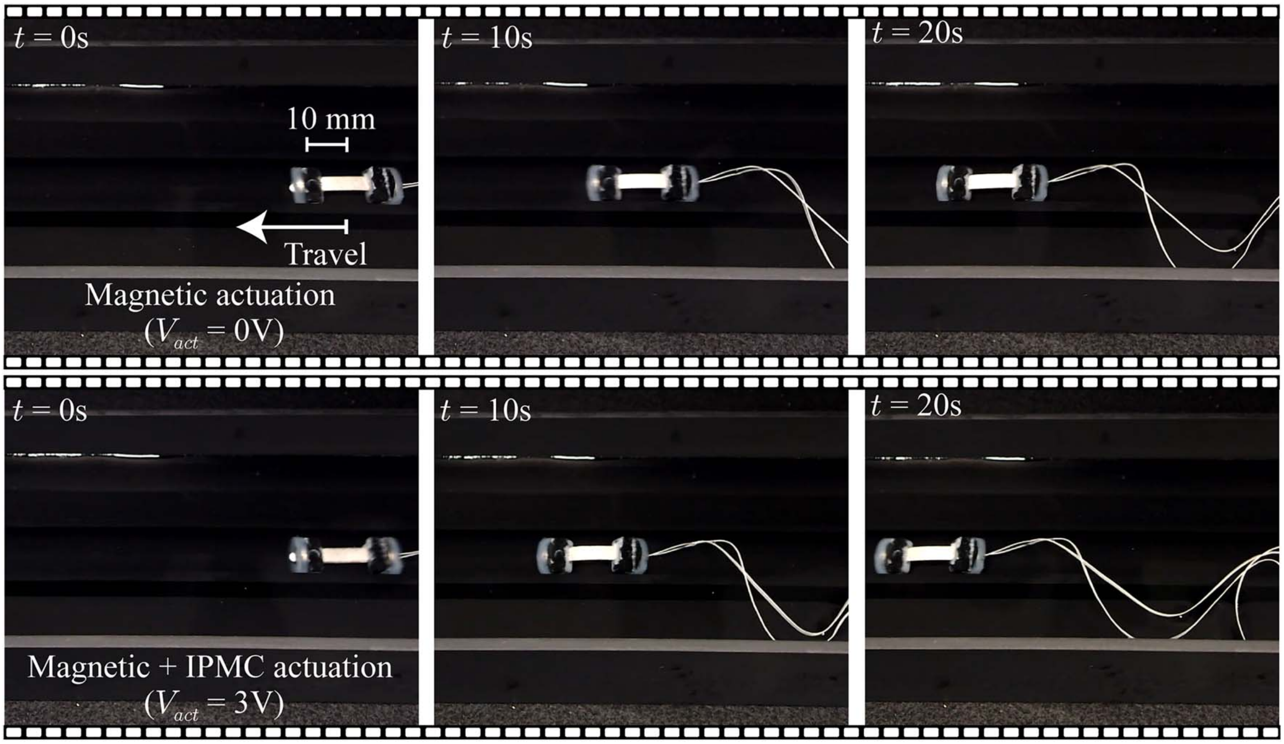

Fig. 6 Time-lapse comparison of the MEESo robot with magnetic actuation (top) and magneto-electroactive actuation (bottom) given a constant voltage ($V_{act} = 3\,\mathrm{V}$) applied to the IPMC body. The trials show that adding EAP body actuation improves the robot's gait over the purely magnetic actuation.

electroactive polymer body of the MEESo robot can improve the traversal speed of the device (Table 1).

Looking at the time to travel 20 mm, the robot with no IPMC actuation takes 9.4 ± 2.7 s. By providing constant DC (+3V) and square-wave actuation signals to the electroactive material, the time to 20 mm is reduced to 3.0 ± 1.1 and 4.7 ± 3.1 s, respectively. These equate to travel time improvements of 68% and 50%. An ANOVA test was run for the three groups in each row. The *p*-value comparing the three groups in the top row is 8.0×10^{-4}. The DC and square-wave trials are significantly different from the no actuation group, but they are not significantly different from each other.

Comparing the travel times of the actuation methods to 40 mm, the following results were obtained: (1) no IPMC actuation took 15.8 ± 3.6 s, (2) DC actuation took 7.9 ± 2.1 s, and (3) square-wave actuation took 10.0 ± 4.1 s. The *p*-value comparing the three groups is 0.0018. Again, the two actuation methods have a statistically significant improvement compared to no IPMC actuation.

For the time each method took to reach 60 mm, the three actuation methods are not significantly different (*p*-value = 0.15). These results show that electroactive actuation can be used to improve the gait of the robot. If the robot's location is accurately known, say ± 2 cm, the improvements of electroactive actuation on the robot's gait compared to a dormant IPMC are significant.

The improvement in travel time of the MEESo robot with IPMC actuation is due to an increase in the step size of the robot's gait compared to purely using magnetic actuation. This is demonstrated for the constant IPMC voltage scenario in Fig. 6. The robot takes larger steps due to increased body deformation from actuating the IPMC. At distances closest to the actuation magnet ($x = 0$), no IPMC actuation results in average step sizes of about 2 mm. A constant IPMC voltage increases the step size of the robot to 6 mm and square-wave excitation to about 4 mm on average.

While IPMC actuation is beneficial to the robot's gait, there are discrepancies between the physical robot and the simulations. The simulation results shown in Fig. 4 predict faster travel than realized in the physical experiment for all the actuation methods tested. These differences are likely due to the ideal assumptions of the simulation. In particular, viscous effects of the aqueous environment are ignored, as well as the additional friction effects introduced by the power tether for the IPMC. Since both of these effects reduce the velocity of the MEESo robot, it is reasonable to expect a 50% or greater reduction in the device's performance in practice, which would result in travel times resembling the experimental results.

Another difference to note is the assumptions made about the IPMC actuation. The IPMC actuation was assumed to be linear and implemented this way in simulation. However, in reality IPMCs have nonlinear responses, such as back relaxation. These are likely additional contributions to the differences between simulation and experimental results. Such behaviors should be included if a simulation environment that estimates realistic velocity values is desired. The focus of this work is to show that IPMC actuation can be used to improve the gait of the robot. The true behavior of IPMC actuation under applied external forces is an open area of research. The simulation was used to examine trends and decide which actuation methods were promising to test with the physical robot.

6 Conclusions

This paper introduced the magneto-electroactive endoluminal soft robot that combines, for the first time, magnetic actuation from an external rotating dipole field with robot-body deformation via an ionic polymer-metal composite actuator. The dual-actuation method enhances locomotion capabilities, specifically through increased control of the body deformation during the gait cycle. The influence of several electroactive actuation methods on the magnetic gait of the robot was explored—both constant and periodic voltage scenarios. A physical dual-actuated MEESo robot was fabricated for testing. It was demonstrated that the magneto-electroactive actuation could beneficially affect the robot's gait compared to magnetic actuation alone, with travel times being decreased by as much as 50–68%. The electroactive actuation allows for greater control of the MEESo robot as it travels through a lumen without changing the magnetic actuation setup.

Acknowledgment

This work was supported by the National Science Foundation under Grant Nos. 1830958 and 1545857. Any opinions, findings, and conclusions or recommendations expressed in this material are those of the authors and do not necessarily reflect the views of the sponsor. Authors also thank Professor Jake Abbott and his group for the insightful technical discussions on magnetic actuation.

Conflict of Interest

There are no conflicts of interest.

Data Availability Statement

The datasets generated and supporting the findings of this article are obtainable from the corresponding author upon reasonable request.

References

[1] Nehme, F., Goyal, H., Perisetti, A., Tharian, B., Sharma, N., Tham, T. C., and Chhabra, R., 2021, "The Evolution of Device-Assisted Enteroscopy: From Sonde Enteroscopy to Motorized Spiral Enteroscopy," Front. Med., **8**, p. 792668.

[2] Li, Z., and Chiu, P. W.-Y., 2018, "Robotic Endoscopy," Visc. Med., **34**(1), pp. 45–51.

[3] Bianchi, F., Masaracchia, A., Shojaei Barjuei, E., Menciassi, A., Arezzo, A., Koulaouzidis, A., Stoyanov, D., Dario, P., and Ciuti, G., 2019, "Localization Strategies for Robotic Endoscopic Capsules: A Review," Exp. Rev. Med. Dev., **16**(5), pp. 381–403.

[4] Verra, M., Firrincieli, A., Chiurazzi, M., Mariani, A., Lo Secco, G., Forcignanò, E., Koulaouzidis, A., Menciassi, A., Dario, P., Ciuti, G., and Arezzo, A., 2020, "Robotic-Assisted Colonoscopy Platform With a Magnetically-Actuated Soft-Tethered Capsule," Cancers, **12**(9), p. 2485.

[5] Kim, S. H., and Chun, H. J., 2021, "Capsule Endoscopy: Pitfalls and Approaches to Overcome," Diagnostics, **11**(10), p. 1765.

[6] Alsunaydih, F. N., and Yuce, M. R., 2021, "Next-Generation Ingestible Devices: Sensing, Locomotion and Navigation," Physiol. Meas., **42**(4), p. 04TR01.

[7] Song, Y., Guo, S., Yin, X., Zhang, L., Hirata, H., Ishihara, H., and Tamiya, T., 2018, "Performance Evaluation of a Robot-Assisted Catheter Operating System With Haptic Feedback," Biomed. Microdev., **20**(2), p. 50.

[8] Zhang, L., Gu, S., Guo, S., and Tamiya, T., 2021, "A Magnetorheological Fluids-Based Robot-Assisted Catheter/Guidewire Surgery System for Endovascular Catheterization," Micromachines, **12**(6), p. 640.

[9] Kaneko, R., Ikeda, H., Uezato, M., and Chin, M., 2022, "Removal of a Central Venous Catheter Penetrating the Vertebral Artery: A Case Report on Endovascular Treatment for Blunt Cerebrovascular Injury," Surg. Neurol. Int., **13**(84), pp. 1–5.

[10] Steiner, J. A., Hussain, O. A., Pham, L. N., Abbott, J. J., and Leang, K. K., 2019, "Toward Magneto-Electroactive Endoluminal Soft (MEESo) Robots," ASME Dynamic Systems and Control Conference (DSCC), DSCC2019-9029, Park City, UT, p. V003T20A002.

[11] Pham, L. N., Steiner, J. A., Leang, K. K., and Abbott, J. J., 2020, "Soft Endoluminal Robots Propelled by Rotating Magnetic Dipole Fields," IEEE Trans. Med. Robot., **2**(4), pp. 598–607.

[12] Huda, M. N., Liu, P., Saha, C., and Yu, H., 2020, "Modelling and Motion Analysis of a Pill-Sized Hybrid Capsule Robot," J. Intell. Robot. Syst., **100**(3), pp. 753–764.

[13] Cheung, E., Karagozler, M. E., Park, S., Kim, B., and Sitti, M., 2005, "A New Endoscopic Microcapsule Robot Using Beetle Inspired Microfibrillar Adhesives," IEEE/ASME International Conference on Advanced Intelligent Mechatronics, Monterey, CA, July 24–28, pp. 551–557.

[14] Carta, R., Sfakiotakis, M., Pateromichelakis, N., Thoné, J., Tsakiris, D. P., and Puers, R., 2011, "A Multi-coil Inductive Powering System for an Endoscopic Capsule With Vibratory Actuation," Sens. Actuat. A Phys., **172**(1), pp. 253–258.

[15] Pancaldi, L., Noseda, L., Dolev, A., Fanelli, A., Ghezzi, D., Petruska, A. J., and Sakar, M. S., 2022, "Locomotion of Sensor-Integrated Soft Robotic Devices Inside Sub-Millimeter Arteries With Impaired Flow Conditions," Adv. Intell. Syst., **4**(5), p. 2100247.

[16] Kim, Y., Parada, G. A., Liu, S., and Zhao, X., 2019, "Ferromagnetic Soft Continuum Robots," Sci. Robot., **4**(33), p. eaax7329.

[17] Thomas, T. L., Venkiteswaran, V. K., Ananthasuresh, G., and Misra, S., 2020, "A Monolithic Compliant Continuum Manipulator: A Proof-of-Concept Study," ASME J. Mech. Rob., **12**(6), p. 061006.

[18] Jeon, S., Hoshiar, A. K., Kim, K., Lee, S., Kim, E., Lee, S., Kim, J.-Y., et al., 2019, "A Magnetically Controlled Soft Microrobot Steering a Guidewire in a Three-Dimensional Phantom Vascular Network," Soft Robot., **6**(1), pp. 54–68.

[19] Jung, E., Nam, J., Lee, W., Kim, J., and Jang, G., 2021, "Crawling Magnetic Robot to Perform a Biopsy in Tubular Environments by Controlling a Magnetic Field," Appl. Sci., **11**(11), p. 5292.

[20] Chi, M., Zhang, J., Liu, R., Wang, Y., Nie, G., and Qian, X., 2021, "Coupled Steering Control of a Low Torsional Torque Capsule Robot in the Intestine," Mechatronics, **77**, p. 102596.

[21] Steiner, J. A., Pham, L. N., Abbott, J. J., and Leang, K. K., 2022, "Modeling and Analysis of a Soft Endoluminal Inchworm Robot Propelled by a Rotating Magnetic Dipole Field," ASME J. Mech. Rob., **14**(5), p. 051002.

[22] Shahinpoor, M., and Kim, K. J., 2004, "Ionic Polymer-Metal Composites: IV. Industrial and Medical Applications," Smart Mater. Struct., **14**(1), p. 197.

[23] Gu, G.-Y., Zhu, J., Zhu, L.-M., and Zhu, X., 2017, "A Survey on Dielectric Elastomer Actuators for Soft Robots," Bioinsp. Biomim., **12**(1), p. 011003.

[24] Tang, C., Du, B., Jiang, S., Wang, Z., Liu, X.-J., and Zhao, H., 2023, "A Review on High-Frequency Dielectric Elastomer Actuators: Materials, Dynamics, and Applications," Adv. Intell. Syst., **6**(2), p. 2300047.

[25] Kellaris, N., Gopaluni Venkata, V., Smith, G. M., Mitchell, S. K., and Keplinger, C., 2018, "Peano-HASEL Actuators: Muscle-Mimetic, Electrohydraulic Transducers That Linearly Contract on Activation," Sci. Robot., **3**(14), p. eaar3276.

[26] Johnson, B., Naris, M., Sundaram, V., Volchko, A., Ly, K., Mitchell, S., Acome, E., et al., 2023, "A Multifunctional Soft Robotic Shape Display With High-Speed Actuation, Sensing, and Control," Nat. Commun., **14**(1), p. 4516.

[27] Bar-Cohen, Y., Leary, S. P., Yavrouian, A., Oguro, K., Tadokoro, S., Harrison, J. S., Smith, J. G., and Su, J., 2000, "Challenges to the Application of IPMC as Actuators of Planetary Mechanisms," *Smart Structures and Materials 2000: Electroactive Polymer Actuators and Devices (EAPAD)*, Vol. 3987, SPIE, Newport Beach, CA, pp. 140–146.

[28] Hamburg, E., Zondaka, Z., Punning, A., Johanson, U., and Aabloo, A., 2016, "Some Electrochemical Aspects of Aqueous Ionic Polymer-Composite Actuators," *Electroactive Polymer Actuators and Devices (EAPAD) 2016*, Vol. 9798, SPIE, Las Vegas, NV, pp. 201–209.

[29] Carrico, J. D., Tyler, T., and Leang, K. K., 2018, "A Comprehensive Review of Select Smart Polymeric and Gel Actuators for Soft Mechatronics and Robotics Applications: Fundamentals, Freeform Fabrication, and Motion Control," Int. J. Smart Nano Mater., **8**(4), pp. 144–213.

[30] Kodaira, A., Asaka, K., Horiuchi, T., Endo, G., Nabae, H., and Suzumori, K., 2019, "IPMC Monolithic Thin Film Robots Fabricated Through a Multi-layer Casting Process," IEEE Robot. Autom. Lett., **4**(2), pp. 1335–1342.

[31] Yi, X., Chakarvarthy, A., and Chen, Z., 2021, "Cooperative Collision Avoidance Control of Servo/IPMC Driven Robotic Fish With Back-Relaxation Effect," IEEE Robot. Autom. Lett., **6**(2), pp. 1816–1823.

[32] Li, J., Tian, A., Sun, Y., Feng, B., Wang, H., and Zhang, X., 2023, "The Development of a Venus Flytrap Inspired Soft Robot Driven by IPMC," J. Bionic Eng., **20**(1), pp. 406–415.

[33] Abdulsadda, A. T., and Tan, X., 2012, "An Artificial Lateral Line System Using IPMC Sensor Arrays," Int. J. Smart Nano Mater., **3**(3), pp. 226–242.

[34] Ming, Y., Yang, Y., Fu, R. P., Lu, C., Zhao, L., Hu, Y. M., Li, C., Wu, Y. X., Liu, H., and Chen, W., 2018, "IPMC Sensor Integrated Smart Glove for Pulse Diagnosis, Braille Recognition, and Human–Computer Interaction," Adv. Mater. Technol., **3**(12), p. 1800257.

[35] Nagel, W. S., Fakharian, O., Aureli, M., and Leang, K. K., 2023, "Engineered IPMC Sensors: Modeling, Characterization, and Application Towards Wearable Postural-Tactile Measurement," Smart Mater. Struct., **33**(1), p. 015035.

[36] Ali, A., Plettenburg, D. H., and Breedveld, P., 2016, "Steerable Catheters in Cardiology: Classifying Steerability and Assessing Future Challenges," IEEE Trans. Biomed. Eng., **63**(4), pp. 679–693.

[37] Fang, B. K., Ju, M. S., and Lin, C. C. K., 2007, "A New Approach to Develop Ionic Polymer-Metal Composites (IPMC) Actuator: Fabrication and Control for Active Catheter Systems," Sens. Actuat. A: Phys., **137**(2), pp. 321–329.

[38] Ruiz, S., Mead, B., Palmre, V., Kim, K. J., and Yim, W., 2015, "A Cylindrical Ionic Polymer-Metal Composite-Based Robotic Catheter Platform: Modeling, Design and Control," Smart Mater. Struct., **24**(4), p. 015007.

[39] Yoon, W. J., Reinhall, P. G., and Seibel, E. J., 2007, "Analysis of Electro-Active Polymer Bending: A Component in a Low Cost Ultrathin Scanning Endoscope," Sens. Actuat. A: Phys., **133**(2), pp. 506–517.

[40] Lu, C., Zhao, L., Hu, Y., and Chen, W., 2018, "A Molecular-Regulation Strategy Towards Low-Voltage Driven, Multi Degree of Freedom IPMC Catheters," Chem. Commun., **54**(63), pp. 8733–8736.

[41] Abbott, J. J., Diller, E., and Petruska, A. J., 2020, "Magnetic Methods in Robotics," Annu. Rev. Control Robot. Auton. Syst., **3**, pp. 57–90.

[42] Petruska, A. J., and Abbott, J. J., 2013, "Optimal Permanent-Magnet Geometries for Dipole Field Approximation," IEEE Trans. Magn., **49**(2), pp. 811–819.

[43] M. Shahinpoor, ed., 2016, *Ionic Polymer Metal Composites (IPMCs)*, Smart Materials Series, Vol. 2, The Royal Society of Chemistry, Cambridge.

[44] Nemat-Nasser, S., and Li, J. Y., 2000, "Electromechanical Response of Ionic Polymer-Metal Composites," J. Appl. Phys., **87**(7), pp. 3321–3331.

[45] Michel, O., 2004, "Webots: Professional Mobile Robot Simulation," J. Adv. Robot. Syst., **1**(1), pp. 39–42.